

# FAST-MEPSA: an optimised and faster version of peak detection algorithm MEPSA

Manuele Maistrello<sup>a,b</sup>, Romain Maccary<sup>a,b</sup>, Cristiano Guidorzi<sup>a,b,c</sup>

<sup>a</sup>*University of Ferrara, Department of Physics and Earth Sciences, via Saragat 1, Ferrara, 44122, , Italy*

<sup>b</sup>*Istituto Nazionale di Astrofisica, Osservatorio di Astrofisica e Scienza dello Spazio di Bologna, via Gobetti 93/3, Bologna, 40129, , Italy*

<sup>c</sup>*Istituto Nazionale di Fisica Nucleare, Sezione di Ferrara, via Saragat 1, Ferrara, 44122, , Italy*

## Abstract

We present **FAST-MEPSA**, an optimised version of the **MEPSA** algorithm developed to detect peaks in uniformly sampled time series affected by uncorrelated Gaussian noise. Although originally conceived for the analysis of gamma-ray burst (GRB) light curves (LCs), **MEPSA** can be readily applied to other transient phenomena. The algorithm scans the input data by applying a set of 39 predefined patterns across multiple timescales. While robust and effective, its computational cost becomes significant at large re-binning factors. To address this, **FAST-MEPSA** introduces a sparser offset-scanning strategy. In parallel, building on **MEPSA**'s flexibility, we introduce a 40th pattern specifically designed to recover a class of elusive peaks that are typically sub-threshold and lie on the rising edge of broader structures—often missed by the original pattern set. Both versions of **FAST-MEPSA**—with 39 and 40 patterns—were validated on simulated GRB LCs. Compared to **MEPSA**, the new implementation achieves a speed-up of nearly a factor 400 at high re-binning factors, with only a minor ( $\sim 4\%$ ) reduction in the number of detected peaks. It retains the same detection efficiency while significantly lowering the false positive rate of low significance. The inclusion of the new pattern increases the recovery of previously undetected and sub-threshold peaks. These improvements make **FAST-MEPSA** an effective tool for large-scale analyses where a robust trade-off between speed, efficiency, and reliability is essential. The adoption of 40 patterns instead of the classical 39 is advisable when an enhanced efficiency in detecting faint events is desired. The code is made publicly available.

## Keywords:

Gamma rays: bursts, Methods: statistical, Design and analysis of algorithms: pattern matching

## 1. Introduction

In the current time-domain era, monitoring how transient astrophysical phenomena vary over time offers key insights into the physical processes driving their emission. These temporal variations span a broad range of timescales, from milliseconds to years or even longer. Among the most energetic and enigmatic stellar-scale explosions, gamma-ray bursts (GRBs)—brief, intense flashes of gamma rays—stand out as exceptional events.

GRB light curves (LCs, i.e. their flux time profiles) encode a wealth of information about the activity and, possibly, the nature of their central engine. Most LCs appear as a sequence of pulses, often grouped into emission episodes and separated by so-called quiescent times. These pulses vary in shape, duration, and intensity, and exhibit no obvious periodicity (Guidorzi et al., 2025). Several models have been proposed to explain this diversity (see Kumar and Zhang 2015 for a review). In particular, whether LCs arise from a common stochastic process remains an open question. A precise characterisation of any such underlying process therefore requires robust peak-detection methods. This underscores the importance of a method capable of reliably identifying as many peaks as possible in observed LCs, while properly accounting for statistical uncertainties.

In this context, Guidorzi (2015, hereafter G15) introduced a well-calibrated peak search algorithm named **MEPSA** (Multiple

Excess Peak Search Algorithm), which has since been widely used to characterise various LC properties—including the minimum variability timescales (Camisasca et al., 2023); the search for periodic activity (Guidorzi et al., 2025); the distribution of the number of peaks per GRB (Guidorzi et al., 2024; Maccary et al., 2024b); the energy of individual pulses (Maccary et al., 2024a); and the waiting time distribution (Guidorzi et al., 2015).

The simultaneous detection of GW 170817 in gravitational waves (Abbott et al., 2017) and GRB 170817A in  $\gamma$  rays (Goldstein et al., 2017; Savchenko et al., 2017) confirmed the long-suspected association between short GRBs and neutron star binary mergers. In this context, Kocevski et al. (2018) and, more recently, Fletcher et al. (2024) jointly analysed *Fermi*/GBM and *Swift*/BAT data in search of sub-threshold GRBs—i.e. events that not initiate an on-board trigger—temporally coincident with LIGO/Virgo compact binary coalescence triggers. These studies leveraged external information from independent detections, highlighting the importance of robust and sensitive algorithms capable of identifying such elusive events.

Motivated by these needs, we present **FAST-MEPSA**, an optimised version of the **MEPSA** algorithm that preserves its operative structure and philosophy. **FAST-MEPSA** has been specifically designed to achieve an optimal balance between computational speed and detection sensitivity, making it particularly suited to large-scale searches. In parallel, we propose a new pattern that,

when added to the 39 already present, contributes to enhance the capability of the code to identify faint and sub-threshold events, that would be mostly missed otherwise.

The main features of the original method are summarised in Section 2.1, while the modifications introduced in `FAST-MEPSA` are described in Section 2.2. In Section 3, we validate the new algorithm and compare its performance with that of the original `MEPSA`. Conclusions are presented in Section 4. The C code and pattern sets are publicly available<sup>1</sup>.

## 2. Algorithm description

### 2.1. The original algorithm

`MEPSA` is designed to identify peaks in a uniformly sampled time series affected by uncorrelated Gaussian noise. Specifically, it applies a set of 39 patterns simultaneously to each bin  $i$  of the input LC. Each pattern  $P_k$  comprises  $n_{k,l}$  leftward and  $n_{k,r}$  rightward bins relative to bin  $i$ . Each of these surrounding bins is assigned a threshold  $v_{k,j}$ , with  $j = 1, \dots, n_{k,l} + n_{k,r}$ . A pattern  $P_k$  is considered fulfilled at bin  $i$  if

$$\begin{cases} r_i - r_j \geq v_{k,(j-i+n_{k,l}+1)} \sigma_{i,j}, & j = i - n_{k,l}, \dots, i - 1, \\ r_i - r_j \geq v_{k,(j-i+n_{k,l})} \sigma_{i,j}, & j = i + 1, \dots, i + n_{k,r}, \end{cases} \quad (1)$$

where  $r_i$  is the rate in bin  $i$ , and  $\sigma_{i,j} = (\sigma_i^2 + \sigma_j^2)^{1/2}$ , with  $\sigma_i$  denoting the statistical noise in bin  $i$ . Bin  $i$  is promoted to a peak candidate if at least one pattern is satisfied.

The same screening criteria are then applied to re-binned versions of the input LC, with the re-binning factor  $F_{\text{reb}}$  increasing linearly up to a maximum value  $F_{\text{reb,m}}$ . Furthermore, for each  $F_{\text{reb}}$ , the algorithm scans all possible offsets of the LC: there are exactly  $F_{\text{reb}}$  distinct starting bins and as many different re-binned profiles. Finally, whenever the same peak candidate is detected multiple times, `MEPSA` performs a cross-check by comparing the detection times and associated timescales, retaining the one with the highest statistical significance.

### 2.2. The faster algorithm

G15 showed that the computational time of `MEPSA` scales approximately as  $F_{\text{reb,m}}^3$  when applied to typical GRB LCs with average SNR and binning times of a few milliseconds. This scaling imposes a practical constrain the maximum re-binning factor that can be adopted. A detailed analysis of their findings reveals that approximately 64% of the peaks detected by `MEPSA` are associated with a re-binning factor less than or equal to 10, while only 0.5% correspond to factors greater than 100.

Guided by these findings, we introduced two key modifications to reduce computational cost. First, we modified the way the re-binning factor increases:

$$F_{\text{reb}}(n) = \begin{cases} n, & 1 \leq n \leq 10, \\ an^2 + bn + c, & 10 < n \leq R, \end{cases} \quad (2)$$

where  $n$  is an integer variable and

$$R = \left\lceil \frac{-b + \sqrt{b^2 - 4a(c - F_{\text{reb,m}})}}{2a} \right\rceil, \quad (3)$$

with  $b = 1 - 20a$  and  $c = 100a$ . These constraints ensure continuity at the transition between the linear and parabolic regimes. As continuity provides only two conditions, one degree of freedom remains for defining the parabolic growth; we set  $a = 1/2$ , which yields:

$$F_{\text{reb}}(n) = \begin{cases} n, & 1 \leq n \leq 10, \\ \frac{1}{2}n^2 - 9n + 50, & 10 < n \leq R. \end{cases} \quad (4)$$

Choosing  $a = 1/2$  ensured that the scanning becomes sparser at higher  $F_{\text{reb}}$ , but not excessively. This choice reduces the computational time without compromising detection efficiency, as discussed in Section 3.

Secondly, we modified the set of LC offsets scanned by the algorithm. Let  $K$  be the smallest integer such that  $K \geq F_{\text{reb}}/10$ . The sequence of scanned offsets  $O_i$  is then defined recursively as:

$$\begin{cases} O_0 = 0, \\ O_{i+1} = O_i + K, \end{cases} \quad (5)$$

with  $i = 0, \dots, \lfloor F_{\text{reb}}/K \rfloor$ , and  $K$  being the step size of the series. With this scheme, the algorithm scans all possible LC offsets up to a re-binning factor of 10, while the scanning becomes progressively sparser for greater  $F_{\text{reb}}$ .

Hereafter, we refer to this faster version of the code as `FAST-MEPSA`.

### 2.2.1. The 40th pattern

Maccary et al. (2024a) showed that around 10% of the pulses in their sample that were visually identified, were missed by `MEPSA`. We carried out a detailed characterisation of this small fraction of elusive peaks to understand whether they share any common traits. Interestingly, most of them occur on the rising part of other longer-lasting structures, and tend to be predominantly sub-threshold, low-SNR pulses. To improve the detection efficiency in such cases, we developed a new pattern specifically designed to model the rising phase of these peaks and maximise their detection rate.

With reference to Table 1 in G15, the corresponding thresholds are reported in Table 1. We tested both `MEPSA` and `FAST-MEPSA` including the new pattern. The results are reported in Section 3.

### 2.3. Data handling

The following points are valid for both `MEPSA` and `FAST-MEPSA`, and discuss the conditions that must be fulfilled by the input data for a correct usage.

<sup>1</sup>[https://www.fe.infn.it/u/guidorzi/new\\_guidorzi\\_files/code.html](https://www.fe.infn.it/u/guidorzi/new_guidorzi_files/code.html)

### 2.3.1. Background subtraction

MEPSA is designed to operate on background-subtracted time profiles. Although this procedure is not directly part of the algorithm, it has to be properly carried out prior to its application. In fact, an inaccurate background estimate can affect the performance: for example, an under-fitting can lead to false positives while an over-fitting to a sensitivity loss. In these cases, a combination of statistical tests, such as  $\chi^2$  and runs tests on the residuals, can identify trends due to poor background modelling. In general, a poor knowledge and/or modelling of background inevitably affects the sensitivity and reliability of any peak detection algorithm.

### 2.3.2. Poisson noise

MEPSA relies on the assumption that the time series is dominated by Gaussian noise. This assumption holds true if the number of counts in each bin is sufficiently high for the Poisson distribution to approach the Gaussian limit. In the low-counting regime, this approximation breaks down, potentially leading to poor performances. In such cases, LCs should be re-binned to a sufficient timescale that ensures the Gaussian limit prior to the algorithm application, provided this does not affect the genuine variability of the signal. When this condition cannot be satisfied, MEPSA can still be adopted if the average counts per bin is a few, provided that a higher value on the SNR threshold is adopted, a practical approach that was occasionally adopted (Guidorzi et al., 2025). Instead, when the regime is highly Poisson and non-Gaussian (that is, less than a few counts per bin), MEPSA should not be applied and other algorithms should be adopted, such as those devised in Guidorzi et al. (2020).

### 2.4. Re-binning factor

The goal of the algorithm is to detect peaks characterised by a wide range of SNR and/or timescales. A common assumption adopted in our previous works, in which we made an extensive use of MEPSA, was to set  $F_{\text{reb,m}} = 256$  for *CGRO*/BATSE and *Swift*/BAT, and  $F_{\text{reb,m}} = 128$  for *Fermi*/GBM. Considering a nominal bin size of 64 ms, these choices correspond to scanning the LCs up a bin-time of 16.384 s and 8.192 s, respectively. A relatively large re-binning factor is crucial to identify peaks that last a correspondingly long time and, as such, do not exceed the SNR threshold if integrated over shorter time intervals.

## 3. Test and validation

We have two alternative codes, MEPSA and FAST-MEPSA, along with two possible sets of patterns, either 39 or 40. Consequently, the user may choose between four different combinations of codes and patterns. Hereafter, we systematically compare and characterise each of these four possible usages.

Both algorithms were tested on the same sample of simulated LCs described in G15. We below summarise the main properties of these time profiles:

- Group 1:  $N_1 = 300$  LCs, each consisting of 5000 bins of 64 ms. The counts in each bin were generated according to a Poisson distribution with expected value

1000 cnts/bin. In this way, the count rate is approximately normally distributed. These profiles are meant to represent background counts from scintillators operating approximately in the 10–1000 keV band, such as *CGRO*/BATSE, *BeppoSAXGRBM*, *Fermi*/GBM, *Insight-HXMT*/HE, and *SVOM*/GRM.

- Group 2:  $N_2 = 100$  LCs, each with 15000 bins of 64 ms. The counts in bin  $i$  were drawn from a normal distribution<sup>2</sup>  $N(0, \sigma_i)$ , with  $\sigma_i$  values taken from a typical mask-weighted *Swift*/BAT GRB LC in the 15–150 keV band, extracted following the standard procedure recommended by the BAT team<sup>3</sup>. As a coded-mask instrument, this case is also representative of *SVOM*/ECLAIR.
- Group 3:  $N_3 = 150$  LCs, each with 15000 bins of 64 ms, populated with pulses of fast-rise exponential-decay (FRED; Norris et al. 1996) shape. Following G15, we assumed fixed values for the peakedness  $\nu = 1.5$ , the rise time  $\sigma_r = 1$  s, and the decay time  $\sigma_d = 3$  s. Based on this assumption, the corresponding full width at half maximum (FWHM) equals  $(\ln 2)^{1/\nu}(\sigma_r + \sigma_d)$ . Pulses within the same LC were generated assuming exponentially distributed waiting times, corresponding to a memoryless Poisson process with constant expected pulse rate per unit time. Specifically, we used a pulse rate ranging from 1/40 up to 1/20 pulses/s. Pulse amplitudes were selected so that the pulse signal-to-noise ratio (SNR) spans the range  $0.5 \lesssim \log(\text{SNR}) \lesssim 2$ . Background was simulated using the same templates as in Group 2.

### 3.1. Computational time

The computational time was estimated using Group 3 LCs. Each algorithm was applied to every LC, and the runtime was recorded. To assess the effectiveness of the modifications introduced in Section 2.2 at high re-binning factors, we set  $F_{\text{reb,m}} = 512$ . The mean runtimes and their associated  $1\sigma$  uncertainties are reported in Table 2, which highlights a reduction in execution time by a factor of approximately 400, regardless of the number of patterns used.

Number of patterns	MEPSA	FAST-MEPSA
39	$(412 \pm 13)$ s	$(0.99 \pm 0.07)$ s
40	$(408 \pm 6)$ s	$(1.02 \pm 0.07)$ s

Table 2: Mean computational time (with  $1\sigma$  uncertainties) for each version of the algorithm, measured on Group 3 LCs.

<sup>2</sup>As a coded-aperture telescope, BAT produces background-subtracted GRB LCs directly (Barthelmy et al., 2005). Moreover, being the result of linear combinations of the counts of many independent detectors, the rates are normally distributed.

<sup>3</sup>[https://swift.gsfc.nasa.gov/analysis/threads/bat\\_threads.html](https://swift.gsfc.nasa.gov/analysis/threads/bat_threads.html)

$k$	$v_{k,l}$	$v_{k,r}$	$v_{k,1}$	$v_{k,2}$	$v_{k,3}$	$v_{k,4}$	$v_{k,5}$	$v_{k,6}$	$v_{k,7}$	$v_{k,8}$	$v_{k,9}$	$v_{k,10}$
40	6	2	3.5	3.0	2.5	2.0	1.5	0.5	0.5	1.5	—	—

Table 1: The 40th pattern.  $v_{k,l}$  and  $v_{k,r}$  indicate the number of bins to the left and right of the  $i$ th bin in the input time series, respectively.

### 3.2. False positive rate

As in G15, we computed the false positive (FP) rate for each algorithm using Group 1 and Group 2 LCs, as these are purely affected by statistical noise and contain no real structures. The results, summarised in Table 3, show that FAST-MEPSA significantly reduces the number of FPs, primarily due to the sparser scanning of the input LC at large re-binning factors. More specifically, the number of FPs drops from 56 to 13 (a 77% reduction) when using 39 patterns, and from 75 to 37 (a 50% reduction) when using 40 patterns.

Number of patterns	MEPSA	FAST-MEPSA
39	$56 (3.7 \times 10^{-5})$	$13 (8.7 \times 10^{-6})$
40	$75 (5.0 \times 10^{-5})$	$37 (2.5 \times 10^{-5})$

Table 3: Number of FPs detected by each version of the algorithm in Group 1 and 2 LCs. The corresponding fraction out of  $1.5 \times 10^6$  scanned bins is reported in brackets.

We also analysed the distribution of FPs among the patterns. Figure 1 shows the cumulative histogram of FPs for all four combinations of codes and patterns. Pattern 40 clearly exhibits the highest FP rate in both MEPSA and FAST-MEPSA. Having said that, the SNR distribution of FPs spans the range  $3 \lesssim \text{SNR} \lesssim 5$ , indicating that all FPs lie in the region where the statistical significance of the pulse is uncertain. A possible way to address this issue is to impose a threshold on the SNR of detected pulses, requiring  $\text{SNR} > 5$ , as it was done in our past investigations already mentioned above.

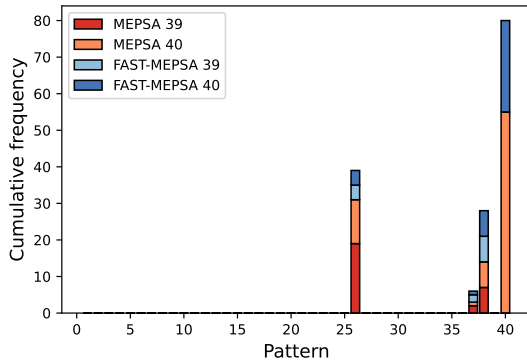


Figure 1: Cumulative histogram of the FPs detected by all four combinations of codes and patterns, as a function of the triggering pattern. Different colours represent the contribution of each algorithm to the total frequency in each histogram bin.

### 3.3. True positive rate

Starting from Group 3 LCs, we computed the true positive (TP) rate for the four algorithm configurations, adopting two

different SNR thresholds:

- Case 1:  $\text{SNR} \geq 5$ , to ensure the statistical significance of the detected peaks;
- Case 2:  $4 \leq \text{SNR} < 5$ , to assess the capability of the 40th pattern to recover peaks falling within the sub-threshold regime.

Number of patterns	MEPSA	FAST-MEPSA
39	29319 (276)	28276 (160)
40	34134 (1294)	33225 (951)

Table 4: Number of TPs with  $\text{SNR} \geq 5$  ( $4 \leq \text{SNR} < 5$ ) detected by each version of the algorithm in Group 3 LCs out of 76970 (8104) simulated peaks.

The results, reported in Table 4, show that FAST-MEPSA leads to a slight reduction in the detection rate: approximately 4% when using 39 patterns, and 3% with 40 patterns. As done for FPs, we also examined the distribution of TPs across patterns. Figure 2 shows the TP spectra: the top panel displays the TP distribution for Case 1, while the bottom panel refers to Case 2. Interestingly, Figure 2 highlights the efficiency of the 40th pattern in detecting peaks in both regimes—particularly in the sub-threshold case, where it recovers a significantly larger fraction of pulses compared to the other patterns.

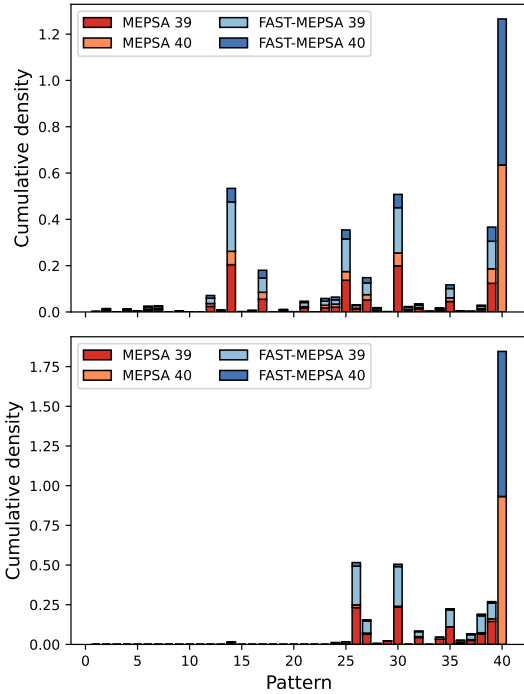


Figure 2: Top panel: Cumulative histogram of TPs with  $\text{SNR} \geq 5$  detected by all four algorithm configurations, as a function of the triggering pattern. Bottom panel: Cumulative histogram of TPs with  $4 \leq \text{SNR} < 5$ . In both panels, different colours represent the contribution of each algorithm to the total frequency in each histogram bin.

### 3.3.1. Efficiency

The efficiency of each algorithm was computed using Group 3 LCs. G15 found that the relevant parameter to detect a given pulse  $i$  is its separability  $s_i$ , defined as:

$$s_i = \frac{\Delta t_{\min,i}}{\text{FWHM}_i}, \quad (6)$$

where  $\Delta t_{\min,i}$  and  $\text{FWHM}_i$  are the pulse's minimum adjacent waiting time and its FWHM, respectively. For a pulse  $i$  peaking at time  $t_{p,i}$ , the minimum waiting time is defined as  $\Delta t_{\min,i} = \min(t_{p,i} - t_{p,i-1}, t_{p,i+1} - t_{p,i})$ . Overall, the separability ranges from  $-3 \lesssim \log(s) \lesssim 2$ . Clearly, the smaller the separability between adjacent pulses, the harder it is for the algorithms to disentangle them, regardless of their SNR.

Following G15, we divided the  $\text{SNR}-s$  plane into 30 bins. In each bin, we computed the efficiency as the fraction of identified peaks over the total number of pulses. Figure 3 compares the four algorithm configurations. The recovered behaviour confirms the findings of G15:

- Efficiency is very high in the top-right region, where pulses are well separated and intense;
- At a given separability, efficiency increases slightly with SNR;
- When  $\log(s) \lesssim -0.4$ , pulses are hardly detected as separate structures, regardless of SNR;

- When  $\log(\text{SNR}) \lesssim 0.7$ , efficiency also drops significantly, nearly independent of separability.

The comparison shown in Figure 3 can be interpreted along both rows and columns:

- Row-wise comparison: the efficiency in the  $\text{SNR}-s$  plane is shown for the same algorithm version, either the original MEPSA or FAST-MEPSA, before and after including the 40th pattern. In both rows, the inclusion of the new pattern visibly enhances the efficiency, particularly in the top right corner and, more generally, in the region within the range  $\log(\text{SNR}) \lesssim 1.5$  and  $\log(s) \lesssim -1$ . This behaviour is expected, since the 40th pattern was specifically designed to recover faint and elusive peaks.
- Column-wise comparison: we compare MEPSA and FAST-MEPSA using the same number of patterns, 39 and 40, respectively. In both cases, the efficiency remains nearly identical, confirming that the modifications introduced in Section 2.2 do not affect the performance.

### 3.3.2. Visually identified missing peaks

We applied MEPSA with pattern 40 to the subset of visually identified peaks from Maccary et al. (2024a) that had been missed by the original pattern set. The inclusion of the new pattern allowed us to recover approximately 30% of these primarily sub-threshold, low-SNR structures.

Figure 4 shows an illustrative example from GRB 180728A. The figure displays the output of MEPSA using 39 patterns, where one peak is clearly missed. The zoomed-in panel shows the same LC analysed with the 40th pattern included: the previously undetected structure is now successfully identified. This example demonstrates the effectiveness of the 40th pattern in capturing elusive peaks that lie on the rising edge of broader emission features.

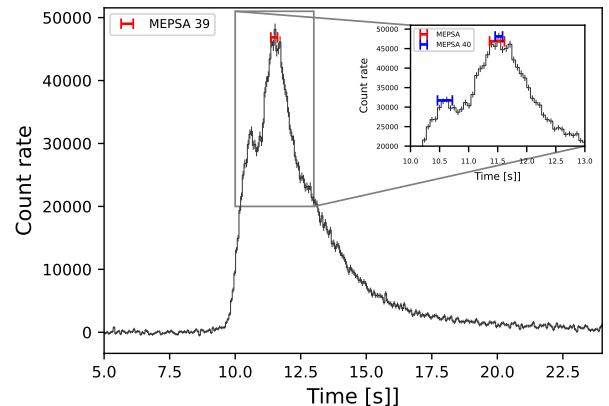


Figure 4: Example of a visually identified peak in GRB 180728A that is missed by MEPSA with 39 patterns and successfully recovered with the inclusion of the 40th pattern. The zoomed-in time interval highlights the peak lying on the rising edge of a broader structure.

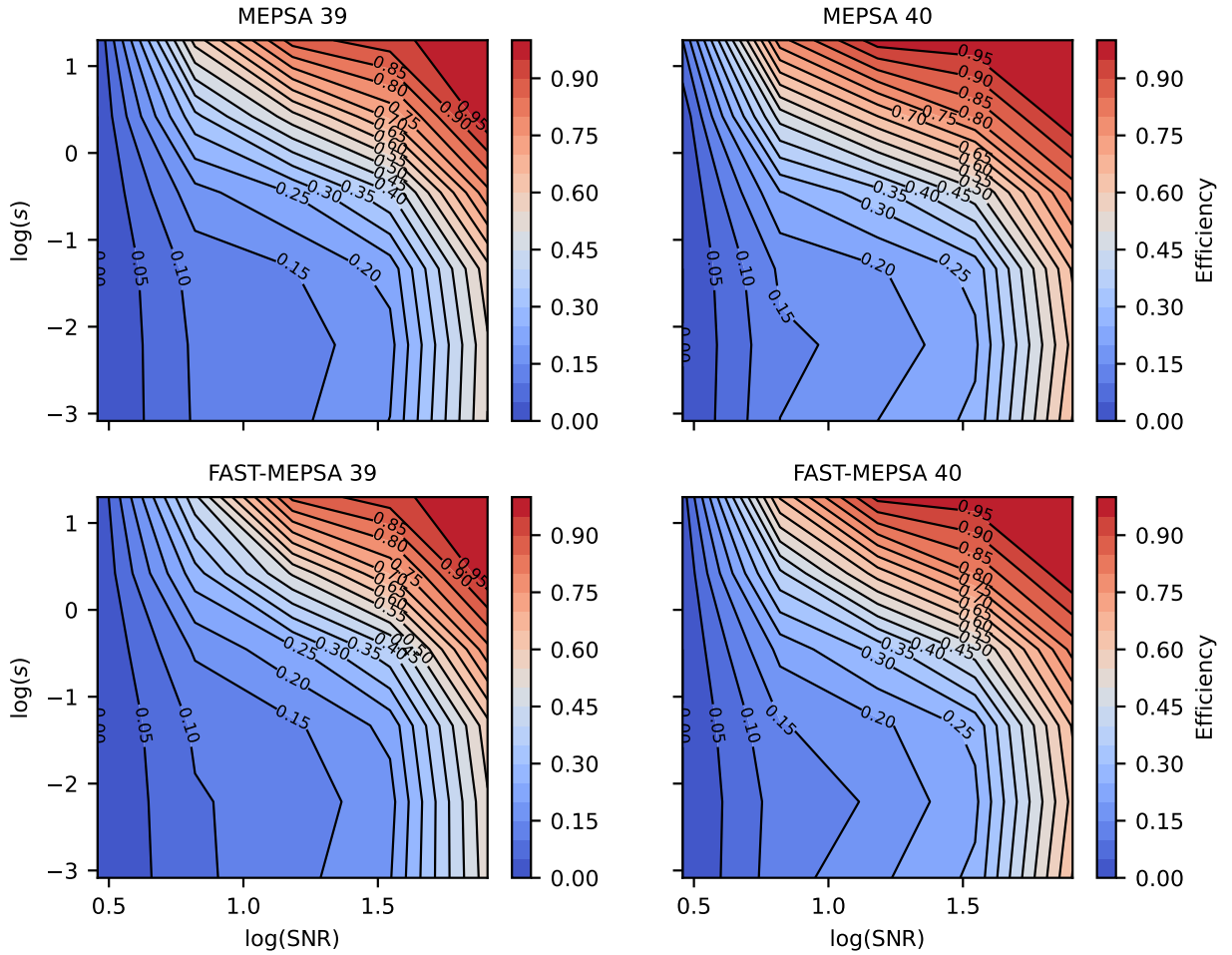


Figure 3: Peak detection efficiency in the SNR–separability plane for MEPSA using 39 patterns (top left), MEPSA using 40 patterns (top right), FAST-MEPSA using 39 patterns (bottom left), and FAST-MEPSA using 40 patterns (bottom right). Different contour levels (from cold to hot colours) correspond to 20 different, equally spaced efficiency levels from 0 to 1.

## 4. Discussion and conclusions

Originally introduced by G15, MEPSA was developed to identify peaks in GRB LCs, although it can be readily applied to other astrophysical transient phenomena. Specifically, MEPSA applies a set of predefined patterns simultaneously to an evenly sampled, background-subtracted input LC affected by uncorrelated Gaussian noise. The same set of patterns is then applied to re-binned versions of the input LC up to a maximum re-binning factor  $F_{\text{reb},m}$ . For each  $F_{\text{reb}}$ , all possible temporal offsets are scanned, resulting in a computational time that scales approximately as  $F_{\text{reb},m}^3$ . This ultimately limits the maximum re-binning factor that can be practically used.

To overcome this limitation, we developed FAST-MEPSA, an optimised version of the original algorithm that preserves its operative structure and philosophy. By adopting a sparser scanning strategy at high re-binning factors, FAST-MEPSA achieves a reduction in computational time of nearly a factor of 400 compared to MEPSA. In parallel, we introduced a new 40<sup>th</sup> pattern, specifically designed to recover a class of elusive and mostly sub-threshold peaks that preferentially lie on the rising edges of broader structures and are often missed by the original set.

We validated both combinations of codes (MEPSA and FAST-MEPSA) with both sets of patterns (39 and 40) on the same set of simulated LCs that had originally been utilised for calibrating MEPSA. Our results show that FAST-MEPSA maintains almost the same detection efficiency as MEPSA, while significantly reducing the false positive (FP) rate thanks to its coarser offset scanning. This comes at the cost of a minor ( $\sim 4\%$ ) reduction in the number of detected peaks. In addition, the introduction of the 40th pattern increased the detection rate, especially for low-SNR, sub-threshold events, demonstrating its usefulness in scenarios where faint signals may carry scientific interest, such as in multi-messenger follow-up searches.

Summing up, we propose a practical set of rules of thumb that may help the user to choose the optimal combination of code and set of patterns that best suites their needs.

- For large-scale analyses over wide datasets—where computational efficiency is crucial—FAST-MEPSA is the best if not the only viable option. An example of application of FAST-MEPSA is offered by its extensive use within a series of simulations based on a genetic algorithm (Maccary et al., submitted). The same recommendation also applies to the cases in which a wide range of timescales is to be scanned, which requires a large value of the maximum rebinning factor.
- When the completeness of the sample of detected peaks is more important than purity, the 40-pattern set should be used instead of the 39-pattern one. This applies independently of the kind of code, either MEPSA or FAST-MEPSA, with the caveat of the previous bullet point (for relatively short LCs and/or relatively small maximum rebin factors, MEPSA is to be preferred over FAST-MEPSA). This is especially the case when the identification of sub-threshold peaks may be relevant.

- When the purity of the sample is to be preferred over its completeness, we recommend to avoid using pattern 40. Concerning the code, there is a slight preference for FAST-MEPSA, given its somewhat lower FP rate.

## Acknowledgements

M.M. and R.M. acknowledge the University of Ferrara for the financial support of their PhD scholarships.

## References

Abbott, B.P., Abbott, R., Abbott, T.D., Acernese, F., Ackley, K., Adams, C., Adams, T., Addesso, P., Adhikari, R.X., Adya, V.B., et al., 2017. Multi-messenger Observations of a Binary Neutron Star Merger. *ApJL* 848, L12. doi:10.3847/2041-8213/aa91c9, arXiv:1710.05833.

Barthelmy, S.D., Barbier, L.M., Cummings, J.R., Fenimore, E.E., Gehrels, N., Hullinger, D., Krimm, H.A., Markwardt, C.B., Palmer, D.M., Parsons, A., Sato, G., Suzuki, M., Takahashi, T., Tashiro, M., Tueller, J., 2005. The Burst Alert Telescope (BAT) on the SWIFT Midex Mission. *Space Sci. Rev.* 120, 143–164. doi:10.1007/s11214-005-5096-3, arXiv:arXiv:astro-ph/0507410.

Camisasca, A.E., Guidorzi, C., Amati, L., Frontera, F., Song, X.Y., Xiao, S., Xiong, S.L., Zhang, S.N., Margutti, R., Kobayashi, S., Mundell, C.G., Ge, M.Y., Gomboc, A., Jia, S.M., Jordana-Mitjans, N., Li, C.K., Li, X.B., Maccary, R., Shrestha, M., Xue, W.C., Zhang, S., 2023. GRB minimum variability timescale with Insight-HXMT and Swift. Implications for progenitor models, dissipation physics, and GRB classifications. *A&A* 671, A112. doi:10.1051/0004-6361/202245657, arXiv:2301.01176.

Fletcher, C., Wood, J., Hamburg, R., Veres, P., Hui, C.M., Bissaldi, E., Briggs, M.S., Burns, E., Cleveland, W.H., Giles, M.M., Goldstein, A., Hristov, B.A., Kocevski, D., Lesage, S., Mailyan, B., Malacaria, C., Poolakkil, S., von Kienlin, A., Wilson-Hodge, C.A., Fermi Gamma-Ray Burst Monitor Team, Crnogorčević, M., Delaunay, J., Tohuvavohu, A., Caputo, R., Cenko, S.B., Laha, S., Parsotan, T., Abbott, R., Abe, H., Acernese, F., Ackley, K., Adhikari, N., Adhikari, R.X., Adkins, V.K., Adya, V.B., Affeldt, C., Agarwal, D., Agathos, M., Agatsuma, K., Aggarwal, N., Aguiar, O.D., Aiello, L., Ain, A., Ajith, P., Akutsu, T., Albanesi, S., Alfaidi, R.A., Allocsa, A., Altin, P.A., Amato, A., Anand, C., Anand, S., Ananyeva, A., Anderson, S.B., Anderson, W.G., Ando, M., Andrade, T., Andres, N., Andrés-Carcasona, M., Andrić, T., Angelova, S.V., Ansoldi, S., Antelis, J.M., Antier, S., Apostolatos, T., Appavuravther, E.Z., Appert, S., Apple, S.K., Arai, K., Araya, A., Araya, M.C., Areeda, J.S., Arène, M., Aritomi, N., Arnaud, N., Arogeti, M., Aronson, S.M., Arun, K.G., Asada, H., Asali, Y., Ashton, G., Aso, Y., Assiduo, M., Assis de Souza Melo, S., Aston, S.M., Astone, P., Aubin, F., Aultoneal, K., Austin, C., Babak, S., Badaracco, F., Bader,

M.K.M., Badger, C., Bae, S., Bae, Y., Baer, A.M., Bagnasco, S., Bai, Y., Baird, J., Bajpai, R., Baka, T., Ball, M., Ballardin, G., Ballmer, S.W., Balsamo, A., Baltus, G., Banagiri, S., Banerjee, B., Bankar, D., Barayoga, J.C., Barbieri, C., Barish, B.C., Barker, D., Barneo, P., Barone, F., Barr, B., Barsotti, L., Barsuglia, M., Barta, D., Bartlett, J., Barton, M.A., Bartos, I., Basak, S., Bassiri, R., Basti, A., Bawaj, M., Bayley, J.C., Bazzan, M., Becher, B.R., Bécsy, B., Bedakihale, V.M., Beirnaert, F., Bejger, M., Belahcene, I., Benedetto, V., Beniwal, D., Benjamin, M.G., Bennett, T.F., Bentley, J.D., Benyaala, M., Bera, S., Berbel, M., Bergamin, F., Berger, B.K., Bernuzzi, S., Berry, C.P.L., Bersanetti, D., Bertolini, A., Betzwieser, J., Beveridge, D., Bhandare, R., Bhandari, A.V., Bhardwaj, U., Bhatt, R., Bhattacharjee, D., Bhaumik, S., Bianchi, A., Bilenko, I.A., Billingsley, G., Bini, S., Birney, R., Birnholtz, O., Biscans, S., Bischi, M., Biscoveanu, S., Bisht, A., Biswas, B., Bitossi, M., Bizouard, M.A., Blackburn, J.K., Blair, C.D., Blair, D.G., Blair, R.M., Bobba, F., Bode, N., Boér, M., Bogaert, G., Boldrini, M., Bolingbroke, G.N., Bonavena, L.D., Bondu, F., Bonilla, E., Bonnand, R., Booker, P., Boom, B.A., Bork, R., Boschi, V., Bose, N., Bose, S., Bossilkov, V., Boudart, V., Bouffanais, Y., Bozzi, A., Bradaschia, C., Brady, P.R., Bramley, A., Branch, A., Branchesi, M., Brau, J.E., Breschi, M., 2024. A Joint Fermi-GBM and Swift-BAT Analysis of Gravitational-wave Candidates from the Third Gravitational-wave Observing Run. *ApJ* 964, 149. doi:10.3847/1538-4357/ad1eed, arXiv:2308.13666.

Goldstein, A., Veres, P., Burns, E., Briggs, M.S., Hamburg, R., Kocevski, D., Wilson-Hodge, C.A., Preece, R.D., Poolakkil, S., Roberts, O.J., Hui, C.M., Connaughton, V., Racusin, J., von Kienlin, A., Dal Canton, T., Christensen, N., Littenberg, T., Siellez, K., Blackburn, L., Broida, J., Bissaldi, E., Cleveland, W.H., Gibby, M.H., Giles, M.M., Kippen, R.M., McBreen, S., McEnerly, J., Meegan, C.A., Paciesas, W.S., Stanbro, M., 2017. An Ordinary Short Gamma-Ray Burst with Extraordinary Implications: Fermi-GBM Detection of GRB 170817A. *ApJL* 848, L14. doi:10.3847/2041-8213/aa8f41, arXiv:1710.05446.

Guidorzi, C., 2015. MEPSA: A flexible peak search algorithm designed for uniformly spaced time series. *Astronomy and Computing* 10, 54–60. doi:10.1016/j.ascom.2015.01.001, arXiv:1501.01117.

Guidorzi, C., Dichiara, S., Frontera, F., Margutti, R., Baldeschchi, A., Amati, L., 2015. A Common Stochastic Process Rules Gamma-Ray Burst Prompt Emission and X-Ray Flares. *ApJ* 801, 57. doi:10.1088/0004-637X/801/1/57, arXiv:1501.02706.

Guidorzi, C., Marongiu, M., Martone, R., Nicastro, L., Xiong, S.L., Liao, J.Y., Li, G., Zhang, S.N., Amati, L., Frontera, F., Orlandini, M., Rosati, P., Virgilli, E., Zhang, S., Bu, Q.C., Cai, C., Cao, X.L., Chang, Z., Chen, G., Chen, L., Chen, T.X., Chen, Y.B., Chen, Y.P., Cui, W., Cui, W.W., Deng, J.K., Dong, Y.W., Du, Y.Y., Fu, M.X., Gao, G.H., Gao, H., Gao, M., Ge, M.Y., Gu, Y.D., Guan, J., Guo, C.C., Han, D.W., Huang, Y., Huo, J., Jia, S.M., Jiang, L.H., Jiang, W.C., Jin, J., Jin, Y.J., Kong, L.D., Li, B., Li, C.K., Li, M.S., Li, T.P., Li, W., Li, X., Li, X.B., Li, X.F., Li, Y.G., Li, Z.W., Liang, X.H., Liu, B.S., Liu, C.Z., Liu, G.Q., Liu, H.W., Liu, X.J., Liu, Y.N., Lu, B., Lu, F.J., Lu, X.F., Luo, Q., Luo, T., Ma, R.C., Ma, X., Meng, B., Nang, Y., Nie, J.Y., Ou, G., Qu, J.L., Sai, N., Shang, R.C., Song, L.M., Song, X.Y., Sun, L., Tan, Y., Tao, L., Tuo, Y.L., Wang, C., Wang, G.F., Wang, J., Wang, W.S., Wang, Y.S., Wen, X.Y., Wu, B.Y., Wu, B.B., Wu, M., Xiao, G.C., Xiao, S., Xu, Y.P., Yang, J.W., Yang, S., Yang, Y.J., Yi, Q.B., Yin, Q.Q., You, Y., Zhang, A.M., Zhang, C.M., Zhang, F., Zhang, H.M., Zhang, J., Zhang, T., Zhang, W.C., Zhang, W., Zhang, W.Z., Zhang, Y., Zhang, Y.F., Zhang, Y.J., Zhang, Y., Zhang, Z., Zhang, Z., Zhang, Z.L., Zhang, H.S., Zhang, X.F., Zheng, S.J., Zhou, D.K., Zhou, J.F., Zhu, Y.X., Zhu, Y., Zhuang, R.L., 2020. A search for prompt  $\gamma$ -ray counterparts to fast radio bursts in the Insight-HXMT data. *A&A* 637, A69. doi:10.1051/0004-6361/202037797, arXiv:2003.10889.

Guidorzi, C., Orlandini, M., Maccary, R., Amati, L., Bazzanini, L., Bulla, M., Ferro, L., Frontera, F., Maistrello, M., Tan, W.J., Tsvetkova, A., Xiong, S.L., Zhang, S.N., 2025. A search for periodic activity in multi-peaked long gamma-ray bursts. *A&A* 697, A228. doi:10.1051/0004-6361/202452326, arXiv:2504.07550.

Guidorzi, C., Sartori, M., Maccary, R., Tsvetkova, A., Amati, L., Bazzanini, L., Bulla, M., Camisasca, A.E., Ferro, L., Frontera, F., Li, C.K., Xiong, S.L., Zhang, S.N., 2024. Distribution of the number of peaks within a long gamma-ray burst. *A&A* 685, A34. doi:10.1051/0004-6361/202449200, arXiv:2402.17282.

Kocevski, D., Burns, E., Goldstein, A., Dal Canton, T., Briggs, M.S., Blackburn, L., Veres, P., Hui, C.M., Hamburg, R., Roberts, O.J., Wilson-Hodge, C.A., Connaughton, V., Racusin, J., Littenberg, T., von Kienlin, A., Bissaldi, E., 2018. Analysis of Sub-threshold Short Gamma-Ray Bursts in Fermi GBM Data. *ApJ* 862, 152. doi:10.3847/1538-4357/aacb7b, arXiv:1806.02378.

Kumar, P., Zhang, B., 2015. The physics of gamma-ray bursts & relativistic jets. *Physics Reports* 561, 1–109. doi:10.1016/j.physrep.2014.09.008, arXiv:1410.0679.

Maccary, R., Guidorzi, C., Amati, L., Bazzanini, L., Bulla, M., Camisasca, A.E., Ferro, L., Frontera, F., Tsvetkova, A., 2024a. Distributions of Energy, Luminosity, Duration, and Waiting Times of Gamma-Ray Burst Pulses with Known Redshift Detected by Fermi/GBM. *ApJ* 965, 72. doi:10.3847/1538-4357/ad26f4, arXiv:2401.14063.

Maccary, R., Maistrello, M., Guidorzi, C., Sartori, M., Amati, L., Bazzanini, L., Bulla, M., Camisasca, A.E., Ferro, L., Frontera, F., Tsvetkova, A., 2024b. Distribution of the number of peaks within a long gamma-ray burst: The

full Fermi/GBM catalogue. *A&A* 688, L8. doi:10.1051/0004-6361/202450666, arXiv:2407.06002.

Norris, J.P., Nemiroff, R.J., Bonnell, J.T., Scargle, J.D., Kouveliotou, C., Paciesas, W.S., Meegan, C.A., Fishman, G.J., 1996. Attributes of Pulses in Long Bright Gamma-Ray Bursts. *ApJ* 459, 393. doi:10.1086/176902.

Savchenko, V., Ferrigno, C., Kuulkers, E., Bazzano, A., Bozzo, E., Brandt, S., Chenevez, J., Courvoisier, T.J.L., Diehl, R., Domingo, A., Hanlon, L., Jourdain, E., von Kienlin, A., Laurent, P., Lebrun, F., Lutovinov, A., Martin-Carrillo, A., Mereghetti, S., Natalucci, L., Rodi, J., Roques, J.P., Sunyaev, R., Ubertini, P., 2017. INTEGRAL Detection of the First Prompt Gamma-Ray Signal Coincident with the Gravitational-wave Event GW170817. *ApJL* 848, L15. doi:10.3847/2041-8213/aa8f94, arXiv:1710.05449.